

SEARCHING FOR DIFFUSE NONTHERMAL X-RAYS FROM THE SUPERBUBBLES N11 AND N51D IN THE LARGE MAGELLANIC CLOUD

H. YAMAGUCHI¹, M. SAWADA², AND A. BAMBA^{3,4}

Draft version November 1, 2018

ABSTRACT

We report on observations of the superbubbles (SBs) N11 and N51D in the Large Magellanic Cloud (LMC) with *Suzaku* and *XMM-Newton*. The interior of both SBs exhibits diffuse X-ray emission, which is well represented by thin thermal plasma models with a temperature of 0.2–0.3 keV. The presence of nonthermal emission, claimed in previous works, is much less evident in our careful investigation. The 3σ upper limits of 2–10 keV flux are 3.6×10^{-14} ergs cm⁻² s⁻¹ and 4.7×10^{-14} ergs cm⁻² s⁻¹ for N11 and N51D, respectively. The previous claims of the detection of nonthermal emission are probably due to the inaccurate estimation of the non X-ray background. We conclude that no credible nonthermal emission has been detected from the SBs in the LMC, with the exception of 30 Dor C.

Subject headings: ISM: bubbles — ISM: individual (N11, N51D) — X-rays: ISM

1. INTRODUCTION

Massive stars are often found clustered in OB associations. Their high-speed stellar winds and the blast wave from core-collapsed supernova (SN) explosions collectively sweep up the ambient interstellar medium (ISM) to generate large (10–100-pc-scale) shell-like structures known as superbubbles (SBs) (e.g., McCray & Snow 1979; Mac Low & McCray 1988). A tenuous cavity created inside an SB shell allows the blast wave of a subsequent supernova remnant (SNR) to propagate rapidly without deceleration for a long time. Furthermore, wind-wind and/or shock-cloud interactions, expected inside an SB, can maintain significant turbulence and magnetic inhomogeneities. Thus, SBs are believed to be very efficient sites for the acceleration of relativistic cosmic rays (e.g., Bykov & Fleishman 1992; Parizot et al. 2004).

The Large Magellanic Cloud (LMC) is particularly suitable for the study of SBs, because of its low foreground extinction (Dickey & Lockman 1990) and its known distance of ~ 50 kpc with a small uncertainty (e.g., Persson et al. 2004). Using *ROSAT*, Chu & Mac Low (1990) and Dunne et al. (2001) systematically studied several SBs in the LMC. They found that the cavities inside the SBs exhibit diffuse X-ray emissions from rarefied hot gas with a temperature on the order of 0.1 keV. They also showed that the X-ray surface brightnesses are significantly higher than those expected from the standard pressure-driven SB model (Weaver et al. 1977). This suggests the presence of interior SNRs colliding with the inner walls of the SB shell.

The detection of nonthermal X-rays has been reported in three LMC SBs, 30 Dor C (Bamba et al. 2004), N11 (Maddox et al. 2009), and N51D (Cooper et al. 2004). 30 Dor C exhibits the nonthermal emission with a clear

shell-like structure. The spectra obtained with *Chandra* and *XMM-Newton* were represented by a power-law with a photon index of $\Gamma = 2\text{--}3$ (Bamba et al. 2004), typical for synchrotron X-rays from nonthermal SNRs. Using *Suzaku*, Yamaguchi et al. (2009) discovered the spectral cutoff in the power-law emission. They concluded that the synchrotron X-rays originate from the rapidly-expanding shell of the SNR with an age of $(4\text{--}20) \times 10^3$ yr.

On the other hand, the validities of the other two results may be doubtful. Maddox et al. (2009) have recently observed N11 with *Suzaku* and have reported the detection of nonthermal X-rays above 2 keV. However, the claimed flux is comparable to that of 30 Dor C despite the fact that no nonthermal component was detected by the previous *XMM-Newton* observation (Nazé et al. 2004). Moreover, a morphology of the emission has been unclear. The *Suzaku* data should be therefore carefully reanalyzed.

The nonthermal emission in N51D is claimed to be distributed entirely in the SB cavity with a centrally peaked morphology in contrast to 30 Dor C (Cooper et al. 2004). The photon index of $\Gamma \sim 1.3$ is much lower than those expected for synchrotron X-rays. On the other hand, in the preceding work by Bomans et al. (2003), the same *XMM-Newton* spectrum was well represented by a thermal plasma model without any additional nonthermal components. Thus, the existence of nonthermal emission in N51D is still controversial. Motivated by this issue, we have obtained a long-time exposure of this SB with *Suzaku*.

The aim of this paper is to investigate for the existence of diffuse hard X-ray emission. Therefore, other properties of SBs and their stellar contents are not focused on. For the analyses, the *Suzaku* data are mainly utilized, since these provide a low and stable non-X-ray background (NXB), particularly for diffuse sources (Mitsuda et al. 2007; Tawa et al. 2008). In addition, we also refer to *XMM-Newton* archival data to compensate the limited angular resolution of *Suzaku*.

First, we briefly introduce the characteristics of N11 (§1.1) and N51D (§1.2). In Section 2, we outline our

hiroya@crab.riken.jp

¹ RIKEN (The Institute of Physical and Chemical Research), 2-1 Hirosawa, Wako, Saitama 351-0198, Japan

² Department of Physics, Kyoto University, Kitashirakawa-oiwake-cho, Sakyo-ku, Kyoto 606-8502, Japan

³ Dublin Institute for Advanced Studies, School of Cosmic Physics, 31 Fitzwilliam Place, Dublin 2, Ireland

⁴ Institute of Space and Astronautical Science, JAXA, 3-1-1 Yoshinodai, Sagami-hara, Kanagawa 229-8510, Japan

TABLE 1
LOG OF OBSERVATIONS APPEARING IN THIS PAPER.

Target name	Telescope/ Instrument	Observation ID	Aim point		Observation start date	Effective exposure (ks)
			α (J2000.0)	δ (J2000.0)		
N11	Suzaku/XIS	501091010	04 ^h 56 ^m 48 ^s	-66°24'38"	2006 Nov 7	30.5
	XMM-Newton/EPIC	0109260201	04 ^h 55 ^m 58 ^s	-66°25'53"	2001 Sep 17	32.5 (MOS)/25.1 (pn)
N51D	Suzaku/XIS	804009010	05 ^h 25 ^m 37 ^s	-67°29'57"	2009 May 17	85.5/87.1/87.3 ^a
	XMM-Newton/EPIC	0071940101	05 ^h 26 ^m 03 ^s	-67°28'52"	2001 Oct 31	30.5 (MOS)/23.1 (pn)
NEP	Suzaku/XIS	500026010	18 ^h 11 ^m 18 ^s	+66°00'45"	2006 Feb 10	88.5

NOTE. — ^aThe exposure times of the XIS0/1/3. The XIS2 was out of operation during this observation.

observation and data reduction procedure. The results for N11 and N51D are presented in Sections 3 and 4, respectively. We discuss our results in Section 5, and give a summary in Section 6. The errors quoted in the text and tables refer to the 90% confidence intervals for one parameter, and the error bars in the figures are for 1σ confidence, unless otherwise stated.

1.1. Characteristics of N11

N11 (DEM L 34), located at the northwest edge of the LMC (Henize 1956), contains four OB associations, LH9, LH10, LH13, and LH14 (Lucke & Hodge 1970). The H α emission exhibits a complex structure consisting of several shells and filaments (e.g., Mac Low et al. 1998). The largest H α shell with a diameter of ~ 120 pc is situated around the central cluster LH9. The age of LH9 is estimated to be ~ 3.5 Myr (Walborn et al. 1999), the oldest among the four clusters. It is suggested that the stellar activity of LH9 triggered a starburst at the periphery, leading to the formation of the other OB associations (e.g., Walborn & Parker 1992; Hatano et al. 2006).

1.2. Characteristics of N51D

N51D (DEM L 192) is located at the southeast corner of the supergiant shell LMC4. Two OB associations, LH51 and LH54 (Lucke & Hodge 1970), are surrounded by a filamentary SB shell with a size of about $140 \text{ pc} \times 120 \text{ pc}$. Both the OB clusters are estimated to have an age of ~ 3 Myr (Oey & Smedley 1998).

2. OBSERVATION AND DATA REDUCTION

2.1. Suzaku

The SBs N11 and N51D were observed with the *Suzaku* X-ray Imaging Spectrometer (XIS; Koyama et al. 2007) on 2006 November 7 and 2009 May 17, respectively. The observation IDs and aim points are summarized in Table 1. The XIS consists of four X-ray charge coupled devices (CCDs). Three of them (XIS0, XIS2, and XIS3) are front-illuminated (FI) and the other (XIS1) is back-illuminated (BI). XIS0, 2, and 3 have a lower and more stable background level for extended emission, while the latter has superior sensitivity in the soft ($\lesssim 1.0$ keV) X-ray band with a significantly improved energy resolution compared with previous X-ray imaging sensors. Combined with X-Ray Telescopes (XRTs; Serlemitsos et al. 2007), the field of view (FOV) of the XIS covers a $\sim 18' \times 18'$ region with a half-power diameter (HPD) of $\sim 2'$. During both the observations, the XIS was operated in the normal full-frame clocking mode with spaced-row charge injection technique. However, the XIS2 was out of operation during the observation of N51D due to damage, possibly caused by the impact of a micro meteorite.

We reduced the data using the standard tools of HEADAS version 6.7. We first employed the revision 2.0 and 2.4 data products for N11 and N51D, respectively. Both were reprocessed using the *xispi* software and the *makepi* files released on 2009 August 13. These files include the latest calibration results for the charge transfer inefficiency and gain. We cleaned the reprocessed data in accordance with the standard screening criteria⁵ and removed flickering pixels. We also excluded time intervals that suffered from telemetry saturation. After the filtering, the effective exposure times were obtained to be ~ 31 ks and ~ 86 ks for the observations of N11 and N51D, respectively. Only grade 0, 2, 3, 4, and 6 events were used in the following analysis.

2.2. XMM-Newton

Detailed information on the *XMM-Newton* observations of both SBs is given in Table 1. The European Photon Imaging Camera (EPIC), aboard *XMM-Newton*, has two Metal Oxide Semiconductor (MOS) CCD arrays (Turner et al. 2001) and one pn CCD array (Strüder et al. 2001). The latter has a higher quantum efficiency than the other CCD arrays. All three cameras have a larger FOV ($\sim 30'$ -diameter circle) than the XIS with a much better HPD of $\sim 6''$ at the optical axis. This makes observations with the EPIC highly sensitive to point-like sources. During both the observations, the MOS and pn CCD arrays were operated in prime full window mode and extended prime full window mode, respectively. Thick filters were used in the observation of N11, while thin ones were used in the observation of N51D.

All the data were processed using version 9.0.0 of the XMM Science Analysis Software (SAS) with the latest calibration files. For the MOS, we selected X-ray events with patterns 0–12, which were passed through the `#XMMEA_EM` filter. For the pn, only events with patterns 0–4 and `flag=0` were extracted. Light curves in the 10–15 keV band, where the effective area of the telescopes rapidly decreases, were accumulated from the whole FOV. To minimize any uncertainty due to the NXB, we removed the periods when the count rate was larger than $0.3 \text{ counts s}^{-1}$ (MOS) and $1.0 \text{ counts s}^{-1}$ (pn). The resultant exposure times are given in Table 1.

3. RESULTS FOR N11

3.1. Images and region selection

Figures 1(a) and 1(b) show XIS images of the N11 region in the soft (0.5–2.0 keV) and hard (2.0–5.0 keV)

⁵ http://heasarc.nasa.gov/docs/suzaku/processing/criteria_xis.html

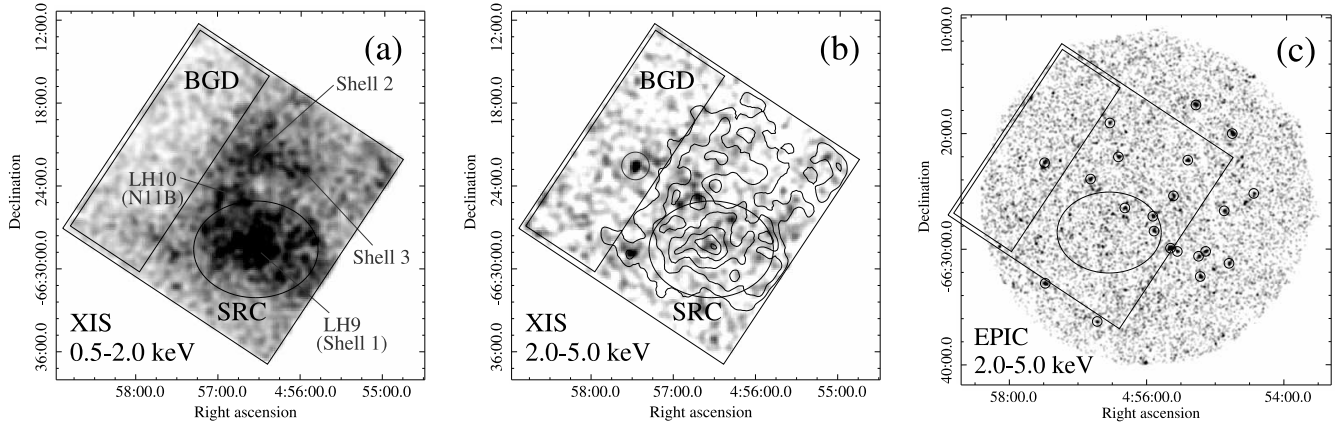


FIG. 1.— Images of N11 SB region, displayed on the J2000.0 coordinates. Panels (a) and (b) are *Suzaku* XIS images in the 0.5–2.0 keV and 2.0–5.0 keV bands, respectively. The latter is overlaid with contours of the former energy band smoothed with a Gaussian kernel of $\sigma = 42''$. The ellipse and rectangle indicate the regions of source (SRC) and background (BGD) spectra, respectively. The small region shown as the gray circle in the panel (b) is excluded from the BGD spectrum. A panel (c) is *XMM-Newton* EPIC-MOS image in the 2.0–5.0 keV band. The FOV of the *Suzaku* XIS and the regions for the spectral analysis are shown. Detected point sources are expressed as the small circles. Note that Shells 1, 2, and 3, labeled in the panel (a), are named by Mac Low et al. (1998).

X-ray bands, respectively. Data from the four detectors were combined. The images were binned by a factor of 8 and smoothed with a Gaussian kernel of $\sigma = 25''$. Extended emission can be clearly seen in the soft-band image, while no significant diffuse structure was found above 2.0 keV.

As already mentioned in previous works (e.g., Nazé et al. 2004), the soft emission peaks near the dense stellar cluster HD 32228 and is widely associated with the OB association LH9. This part is confined by the largest H α shell of the N11 complex (Mac Low et al. 1998), and thus it is considered that the soft X-rays originate from hot shocked gas within the SB shell that is blown by the cluster of stars. The emission is further extended to the north of LH9, the HII region N11B, and shells 2 and 3 (see also Figure 3 of Mac Low et al. 1998). The X-rays from N11B are probably powered by stellar winds from the central young OB stars of LH10. Shells 2 and 3 lie to the north and northwest of N11B, respectively. These X-ray emissions with relatively low surface brightnesses are confined by the faint H α filaments.

Maddox et al. (2009) claimed that nonthermal X-rays had been detected from the region around LH9. Therefore, we concentrate on the spectral analysis of the same region, an ellipse containing the entire SB around LH9 with major and minor radii of $4'.5$ and $3'.5$, respectively—hereafter, “SRC”. The background (BGD) for the SRC spectra was taken from an off-source region, the rectangle shown in Figure 1, but the CCD corners were excluded to remove X-rays from the calibration sources.

A high-resolution EPIC image in the hard band is shown in Figure 1(c). This image was made by merging two MOS images binned by a factor of 32 and smoothed with a Gaussian profile of $\sigma = 9''.6$. Similarly to the XIS image for the same energies (Figure 1b), no extended emission was observed in the EPIC FOV. Point source extraction was performed using the `ewavelet` task of SAS with a detection threshold of 5σ . The positions of the detected sources are indicated with small circles in the figure. Three discrete sources are located in the SRC region, while one is located in the BGD region. The latter,

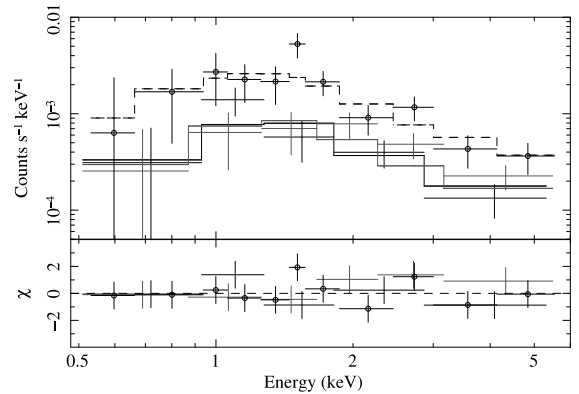


FIG. 2.— Integrated EPIC spectra of three point sources included within the N11 SRC region. MOS1 (black), MOS2 (gray), and pn (black with circles) spectra are simultaneously fitted with an absorbed power-law model shown with solid and dashed lines.

at (R.A., Decl.) = ($4^{\text{h}}57^{\text{m}}28^{\text{s}}$, $-66^{\circ}22'40''$), is known to be associated with the cluster HD 268743, or Sk-66 $^{\circ}$ 41 (Nazé et al. 2004). Since this source is also clearly visible in the XIS image, we excluded it from the BGD region for spectral analysis.

3.2. *XMM-Newton* spectra of point-like sources

Here we analyze the EPIC data of the resolved point sources to take into account their contribution to the hard X-ray flux from the SRC region. Figure 2 shows the background-subtracted EPIC spectra, where the three point sources in the SRC region are merged to improve the statistics. The spectrum of each point source was extracted from the circular region with a radius of $15''$, while the background was taken from an annulus with inner and outer radii of $15''$ and $60''$, respectively.

The spectra were phenomenologically fitted with an absorbed power-law model. The absorption cross sections were taken from Morrison & McCammon (1983). The elemental abundances were assumed to be the values in Anders & Grevesse (1989). The fit was acceptable ($\chi^2/\text{dof} = 15/19$) with $N_{\text{H}} = 2.9$ (1.1–7.8)

TABLE 2
2–10 keV SURFACES BRIGHTNESSES OF N11 AND NEP REGIONS.

	Solid angle (arcmin ²)	Flux [2–10 keV] ($\times 10^{-13}$ ergs cm ⁻² s ⁻¹)	Surface brightness [2–10 keV] ($\times 10^{-15}$ ergs cm ⁻² s ⁻¹ arcmin ⁻²)
SRC	49.4	2.2 (2.0–2.4)	4.4 (4.0–4.8)
(point sources (subtracted))		0.36 (0.31–0.41)	—
BGD	70.4	1.8 (1.6–2.0)	3.6 (3.2–4.1)
		2.8 (2.5–3.1)	4.0 (3.6–4.4)
NEP	113.1	5.0 (4.8–5.1)	4.4 (4.2–4.5)

NOTE. — The NXB is subtracted from each region, but the CXB is still included.

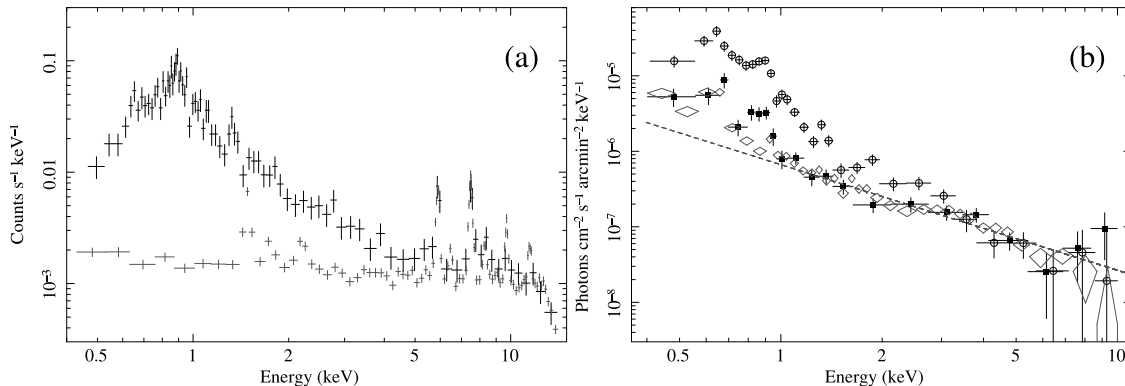


FIG. 3.— (a) XIS0 raw spectrum of the N11 SRC region (black) and NXB spectrum generated by `xisnxbgen` software (gray). (b) NXB-subtracted photon spectra of the SRC (open circle) and BGD (filled square) regions, normalized by each solid angle. For comparison, the same spectrum from the NEP are shown with gray diamonds. The dashed line indicates a power-law with photon index of 1.4, a typical value for the cosmic X-ray background.

$\times 10^{21}$ cm⁻² and $\Gamma = 1.5$ (1.1–2.2). The observed flux in the 2–10 keV band was obtained to be 3.6 (3.1–4.1) $\times 10^{-14}$ ergs cm⁻² s⁻¹.

3.3. *Suzaku* spectra of extended emission

Since the emission from the SRC region is faint, background reduction should be carefully performed to obtain an accurate result. We first subtract the NXB from the SRC and BGD raw spectra, and examine the difference in the hard X-ray fluxes between them (Section 3.3.1). Then, we subtract the other background components, such as the cosmic X-ray background (CXB) and local emission, and perform model fittings to the SRC spectrum (Section 3.3.2).

3.3.1. Search for hard X-rays

Figure 3(a) shows the XIS0 raw spectrum of the SRC region. Instrumental emission lines of Mn-K α , Ni-K α and K β , and Au-L α can be observed at ~ 5.9 keV, ~ 7.5 keV, ~ 8.3 keV, and ~ 9.7 keV, respectively. Using `xisnxbgen` software, we constructed the NXB spectrum from the night-Earth database. This was extracted from the same detector coordinates to the SRC region and sorted with the geomagnetic cut off rigidity for reproducibility. The intensities of the Ni-K α lines were found to be 1.6 (1.1–2.1) $\times 10^{-3}$ counts s⁻¹ and 1.6 (1.5–1.7) $\times 10^{-3}$ counts s⁻¹ for the raw SRC and NXB spectra, respectively. Since these are highly consistent with each other, we can consider that the NXB spectrum was correctly reproduced. The NXB for the BGD spectrum was also successfully constructed by the same method.

After the NXB subtraction, the surface brightness spectra of the SRC and BGD regions were obtained as

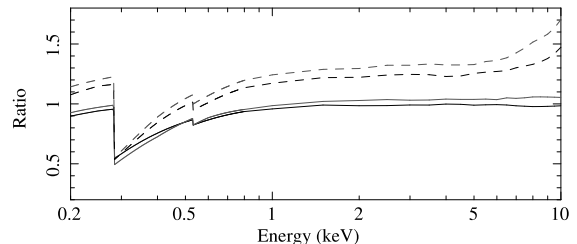


FIG. 4.— Effective-area ratios between the SRC and BGD regions, used for the vignetting correction. Solid black, solid gray, dashed black, and dashed gray represent XRT0, XRT1, XRT2, and XRT3, respectively.

shown in Figure 3(b) (shown as circles and squares, respectively). For comparison, we also present the spectrum of another source-free region (shown as gray diamonds), taken from the observation of the north ecliptic pole (NEP). All the spectra are similar to each other at energies above ~ 3 keV, suggesting that the hard X-rays from the SRC region are dominated by the CXB. Table 2 gives the 2–10 keV surface brightness of each region, determined using the data of all four XIS. No excess SRC flux was found.

3.3.2. Spectral fitting

The spectrum of the BGD region was subtracted from the SRC spectrum. However, since the vignetting of the *Suzaku* XRT significantly decreases the effective area at large off-axis positions (Serlemitsos et al. 2007), the BGD spectrum $I_B(E)$ was corrected before the subtraction as

$$I'_B(E) = I_B(E) \cdot \frac{\Omega_S}{\Omega_B} \cdot f(E), \quad (1)$$

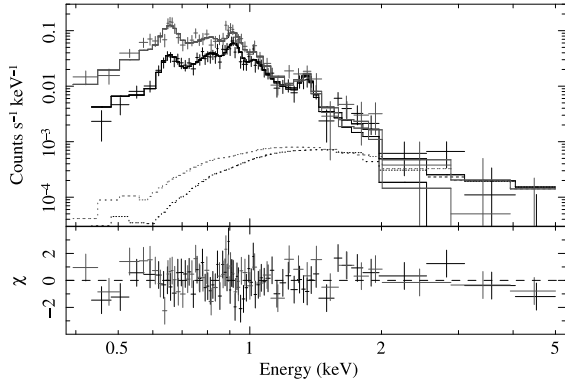


FIG. 5.— Background-subtracted XIS spectra of N11, fitted with an APEC model (solid lines). Black and gray represent FI and BI, respectively. Contribution of the point sources determined from the EPIC spectra is given with the dotted lines.

TABLE 3
BEST-FIT SPECTRAL PARAMETERS FOR N11.

Parameter	Value
N_{H}^{G} (cm^{-2}) ^a	4.3×10^{20} (fixed)
$N_{\text{H}}^{\text{LMC}}$ (cm^{-2}) ^a	$< 2.3 \times 10^{21}$
kT_e (keV)	0.30 (0.28–0.32)
O (solar)	0.26 (0.15–0.47)
Ne (solar)	0.39 (0.20–0.47)
Mg (solar)	0.43 (0.22–0.89)
Fe (solar)	0.12 (0.08–0.22)
$n_e n_p V$ (cm^{-3})	$5.4 (2.6\text{--}19) \times 10^{58}$
$F_{\text{X}}^{\text{obs}}$ ($\text{ergs cm}^{-2} \text{ s}^{-1}$) ^b	4.9×10^{-13}
L_{X} (ergs s^{-1}) ^b	2.2×10^{35}
χ^2/dof	99/105 = 0.94

NOTE. — ^aAbsorption column in the Galaxy and LMC, where the solar and LMC abundances are respectively assumed. ^bObserved flux and luminosity in the 0.5–2.0 keV band.

where Ω_{S} and Ω_{B} are the solid angles of the SRC and BGD regions. The correction factor $f(E)$ is the energy-dependent effective-area ratio between the SRC and BGD regions. Using `xissim` software, we estimated the $f(E)$ values for each XRT as given in Figure 4. This estimation also takes into account the contaminating material built up on the optical blocking filters of the XIS (Koyama et al. 2007). The differences in the results among the telescopes are mainly due to the scattering of the optical axes of the XRTs (see Figure 8 of Serlemitsos et al. 2007).

The BGD-subtracted SRC spectra are shown in Figure 5. The data from three FIs were combined because their response characteristics are almost identical. No significant signal was detected in the energy band above ~ 3 keV, which is consistent with the result in Section 3.3.1. K-shell emission lines of O VIII (~ 0.65 keV), Ne IX (~ 0.91 keV), and Mg XI (~ 1.34 keV) were clearly separate, indicating a thermal origin of the soft X-rays. Thus, we fitted the spectra with an optically thin thermal plasma model (APEC: Smith et al. 2001). The electron temperature (kT_e) and emission measure ($n_e n_p V$, where n_e , n_p , and V are the electron and proton densities, and the emitting volume, respectively) were treated as free parameters. The elemental abundances relative to solar values (Anders & Grevesse 1989) were fixed to the mean LMC values of Russell & Dopita

(1992), but the Mg and Si abundances were assumed to be those of Hughes et al. (1998) since the values from Russell & Dopita (1992) were more uncertain. The interstellar extinction in the Galaxy and LMC were separately considered. The Galactic absorption column density with the solar abundances was fixed to be $N_{\text{H}}^{\text{G}} = 4.3 \times 10^{20} \text{ cm}^{-2}$ (Dickey & Lockman 1990). The other component ($N_{\text{H}}^{\text{LMC}}$) was a free parameter, with the assumption of the LMC metal abundances. In addition, the point source model derived in Section 3.2 was given as a fixed component (with an independent absorption column). This model gave a best fit with $kT_e = 0.18$ (0.17–0.19) keV and $\chi^2/\text{dof} = 144/109$.

We next allowed the abundances of O, Ne, Mg, and Fe to vary freely (by using a VAPEC model). Then, we obtained a significantly improved fit with $\chi^2/\text{dof} = 99/105$. The best-fit parameters are given in Table 3. The Fe abundance was found to be slightly lower than the mean LMC value (~ 0.3 solar: Russell & Dopita 1992; Hughes et al. 1998). The observed flux of $4.9 \times 10^{-13} \text{ ergs cm}^{-2} \text{ s}^{-1}$ (in the 0.5–2.0 keV band) is comparable with the result of Nazé et al. (2004) but inconsistent with that of Maddox et al. (2009) ($\sim 2.5 \times 10^{-13} \text{ ergs cm}^{-2} \text{ s}^{-1}$), although the same data were analyzed.

The derived electron temperature was slightly higher than the values in previous reports (~ 0.2 keV: Dunne et al. 2001; Nazé et al. 2004; Maddox et al. 2009). We found, however, that the fit with a fixed kT_e of 0.2 keV also yielded an acceptable χ^2/dof value of 111/106. This temperature difference does not severely affect the flux in the hard (> 2 keV) X-ray band.

4. RESULTS FOR N51D

4.1. Images and region selection

X-ray images of the N51D region are shown in Figure 6 for the XIS soft X-ray band (a), the XIS hard X-ray band (b), and the EPIC hard X-ray band (c). The binning factors and smoothing Gaussian kernels are same as those used in Figure 1. Similarly to N11, the diffuse structure was only observed in the soft-band image. The bright soft emission is coincident with the OB association LH54 and is surrounded by the N51D $\text{H}\alpha$ shell (see also Figure 1 of Cooper et al. 2004).

The SRC region was selected to be the same as that in Cooper et al. (2004): an ellipse with major and minor radii of $5.8'$ and $4'$, respectively, and a $4' \times 4'$ -square, indicated in Figure 6. Although a small circular region around the Wolf-Rayet star HD 36402 was excluded from the spectral analysis in the previous work, here we included this region because no local structures were resolved in the low-resolution XIS image. The BGD region was selected to be an off-source polygonal region, but the CCD corner irradiated by the calibration sources was excluded.

Using the EPIC image (Figure 6c), we searched for hard discrete sources. As a result, ten sources were detected in the SRC region, while no point source was found in the BGD region. These sources were not clearly resolved in the XIS image. Therefore, we first analyzed the EPIC spectra of the point sources and then performed a model fit to the XIS data in the SRC region by adding the point-source component as a fixed model.

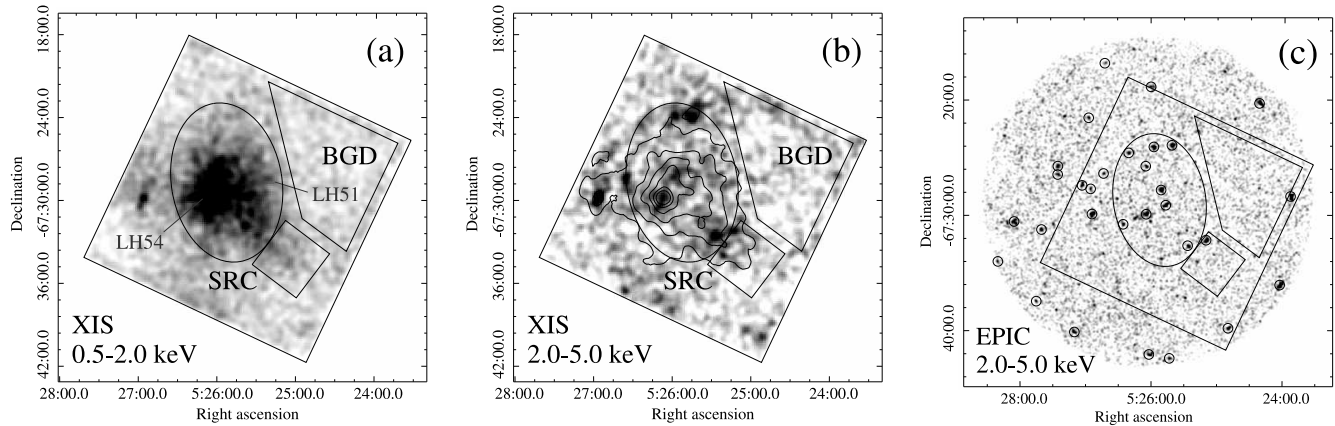


FIG. 6.— Same as Figure 1, but for the N51D region. The ellipse and square are the source (SRC) regions for the diffuse spectrum, whereas the polygon indicates the background (BGD) region.

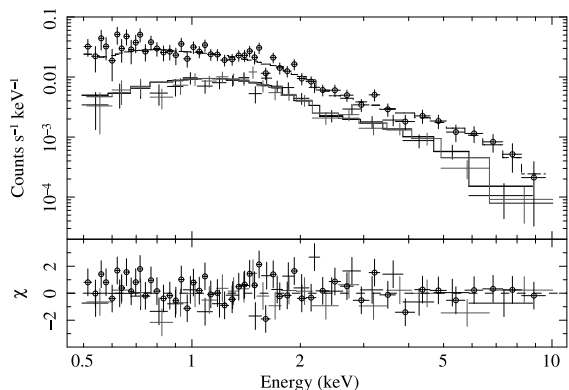


FIG. 7.— Same as Figure 2, but for N51D. Ten point sources within the SRC region are integrated.

TABLE 4
FLUX DISTRIBUTION OF THE POINT SOURCES WITHIN THE N51D SRC REGION.

Flux	Number
0.5–1.0	2
1.0–2.0	3
2.0–4.0	4
4.0–6.0	1

NOTE. — Observed fluxes are given in the spectral range of 2–10 keV, and in unit of 10^{-14} ergs cm^{-2} s^{-1} .

4.2. XMM-Newton spectra of point-like sources

EPIC spectra of the ten point sources in the SRC region were extracted and integrated. The background spectra were extracted from an annular region around each point source. The resultant background-subtracted spectra are shown in Figure 7. The spectra were well reproduced with an absorption power-law model ($\chi^2/\text{dof} = 81/94$). The best-fit absorption column and photon index were $N_{\text{H}} = 1.3$ (0.87–1.8) $\times 10^{21}$ cm^{-2} and $\Gamma = 1.7$ (1.6–1.8), respectively. The observed flux was obtained to be 2.4 (2.3–2.5) $\times 10^{-13}$ ergs cm^{-2} s^{-1} in the 2–10 keV band. The flux distribution of the ten sources is given in Table 4.

4.3. Suzaku spectra of extended emission

The spectral analysis of the *Suzaku* data was performed by essentially the same procedure as that described in Section 3.3. An example of a raw spectrum in the SRC region and the corresponding NXB are compared in Figure 8(a). Given that both spectra exhibit the same intensity of each fluorescent line, we considered that the NXB was successfully constructed. The NXB-subtracted spectra and the 2–10 keV surface brightnesses of the SRC and BGD regions were obtained as shown in Figure 8(b) and Table 5, respectively. The SRC spectrum appears to show excess surface brightness in the hard X-ray band. However, upon subtracting the point-source flux from the SRC, we found that the remaining surface brightness is consistent with that in the BGD region.

We applied the vignetting correction to the BGD spectra and then subtracted them from the SRC spectra. The correction factors $f(E)$ were obtained as given in Figure 9. The resultant SRC spectra are shown in Figure 10. The spectra of two active FIs were merged to improve the photon statistics. Several emission lines can be observed below ~ 1 keV, while the spectrum in the hard band is featureless. Therefore, we fitted the spectrum with a VAPEC model plus the point-source component (a power-law) derived in Section 4.2. The elemental abundances except for those of O, Ne, and Fe were fixed to the LMC values (Russell & Dopita 1992; Hughes et al. 1998). We assumed the Galactic absorption column to be $N_{\text{H}}^{\text{G}} = 6.0 \times 10^{20}$ cm^{-2} , in accordance with Dickey & Lockman (1990). The fit was acceptable with $\chi^2/\text{dof} = 92/103$. The best-fit parameters and models are respectively shown in Table 6 and in Figure 10 with solid and dotted lines. Note that the point-source component was not fitted here. The model successfully reproduced the spectral shape as well as the flux of the hard X-rays, and hence no additional nonthermal component was required to improve the fit.

Cooper et al. (2004) argued that the EPIC spectrum of the diffuse emission exhibited thermal and nonthermal components, and the former accounted for $\sim 70\%$ of the total observed flux (in the 0.3–3.0 keV band) of 1.1×10^{-12} ergs cm^{-2} s^{-1} . With the given temperature and absorption column, the flux of the thermal emission was calculated to be $\sim 6 \times 10^{-13}$ ergs cm^{-2} s^{-1} in the 0.5–

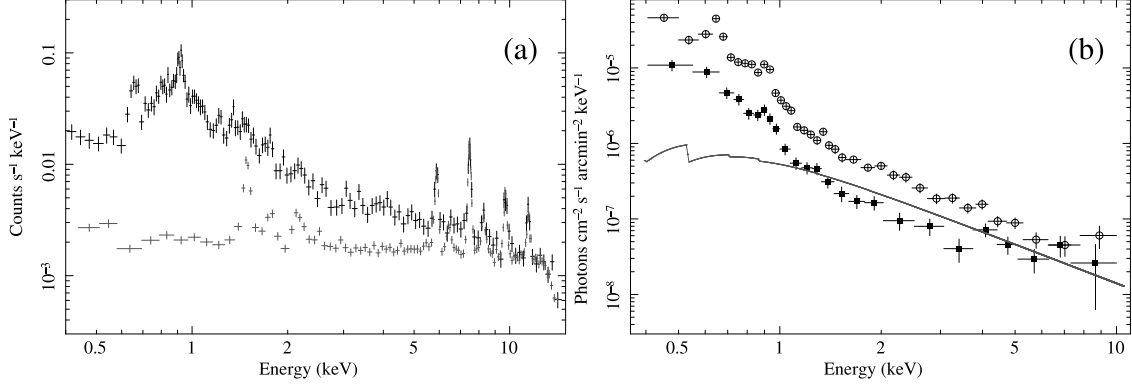


FIG. 8.— Same as Figure 3, but for N51D. The gray curve in the panel (b) indicates the spectral model for the point sources derived by the EPIC spectra (Figure 7).

TABLE 5
2–10 keV SURFACES BRIGHTNESSES OF N51D REGION.

	Solid angle (arcmin ²)	Flux [2–10 keV] ($\times 10^{-13}$ ergs cm ⁻² s ⁻¹)	Surface brightness [2–10 keV] ($\times 10^{-15}$ ergs cm ⁻² s ⁻¹ arcmin ⁻²)
SRC	88.9	5.2 (5.0–5.4)	5.9 (5.6–6.1)
(point sources)		2.4 (2.3–2.5)	—
(subtracted)		2.8 (2.5–3.0)	3.1 (2.9–3.4)
BGD	48.4	1.7 (1.5–1.9)	3.5 (3.1–3.9)

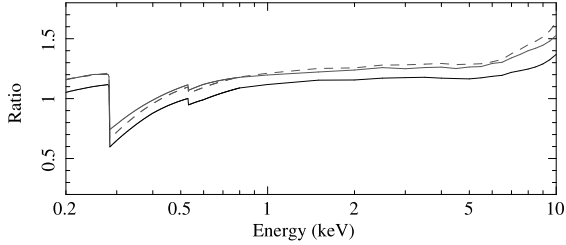


FIG. 9.— Same as Figure 9, but for the observation of N51D.

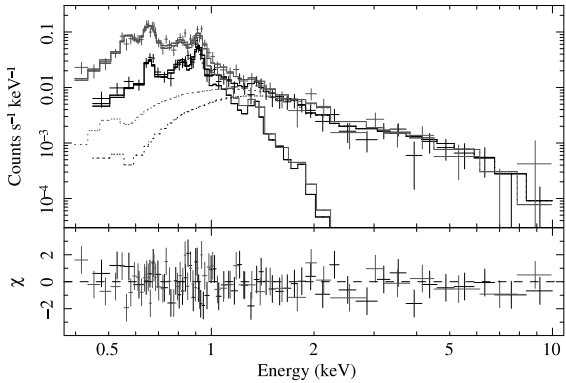


FIG. 10.— XIS spectra of N51D, fitted with an APEC model (solid lines). Black and gray represent FI and BI, respectively. The dotted lines represent the spectra of the point sources.

2.0 keV band. This is comparable to our result.

The enhancement of O and/or Ne abundances was reported in the works of Bomans et al. (2003) and Cooper et al. (2004). On the other hand, our spectrum does not show any evidence of a significant deviation

TABLE 6
BEST-FIT SPECTRAL PARAMETERS FOR N51D.

Parameter	value
N_{H}^{G} (cm ⁻²)	6.0×10^{20} (fixed)
$N_{\text{H}}^{\text{LMC}}$ (cm ⁻²)	$< 5.2 \times 10^{20}$
kT_e (keV)	0.22 (0.20–0.23)
O (solar)	0.14 (0.11–0.21)
Ne (solar)	0.35 (0.26–0.49)
Fe (solar)	0.18 (0.12–0.27)
$n_e n_p V$ (cm ⁻³)	$9.8 (7.0\text{--}14) \times 10^{58}$
F_X^{obs} (ergs cm ⁻² s ⁻¹)	5.6×10^{-13}
L_X (ergs s ⁻¹)	2.4×10^{35}
χ^2/dof	92/103 = 0.89

from the typical LMC abundances, suggesting that the hot gas mainly originates from ISM with only slight enrichment by SN ejecta.

5. DISCUSSION

The X-ray spectra of the SBs N11 and N51D are well reproduced by single-component thin-thermal plasmas (with the models for the group of point sources). Figure 11 shows the unfolded spectra of both SBs. The presence of additional nonthermal emission, argued in previous works (N11: Maddox et al. 2009; N51D: Cooper et al. 2004), is much less evident in our detailed analyses, supporting the earlier results by Nazé et al. (2004) and Bomans et al. (2003). The 2–10 keV flux of the diffuse component F_{D} ($\pm \sigma_{\text{D}}$) for each SB can be calculated as

$$F_{\text{D}} = \left[F_{\text{S}} - F_{\text{PS}} - \frac{\Omega_{\text{S}}}{\Omega_{\text{B}}} \cdot F_{\text{B}} \right] \pm \sigma_{\text{D}} \quad (2)$$

$$\sigma_{\text{D}} = \left[\sigma_{\text{S}}^2 + \sigma_{\text{PS}}^2 + \left(\frac{\Omega_{\text{S}}}{\Omega_{\text{B}}} \right)^2 \sigma_{\text{B}}^2 \right]^{1/2}, \quad (3)$$

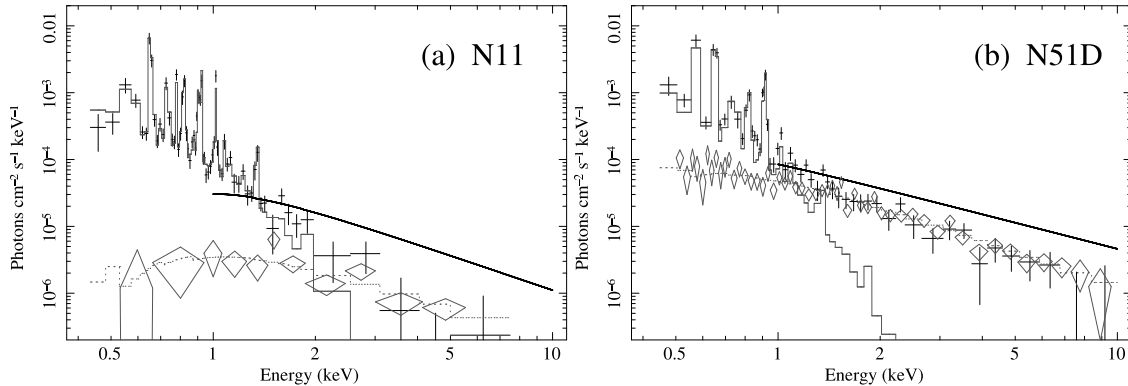


FIG. 11.— XIS-FI unfolded spectra (black crosses) of N11 (a) and N51D (b). The EPIC-pn spectra of the point sources are also shown with gray diamonds. Solid and dashed gray lines are the model components of the diffuse and point sources, respectively. The spectra of “nonthermal emission” claimed by Maddox et al. (2009) and Cooper et al. (2004) (for N11 and N51D, respectively) are indicated with the black thick lines. The data points in the energies above ~ 2 keV are obviously far below the claimed fluxes although the point sources are not subtracted from the XIS spectra.

where F_S , F_B , and F_{PS} (and σ_S , σ_B , σ_{PS}) are the 2–10 keV fluxes (and uncertainties) of the SRC and BGD regions and that of the point sources. Using the values given in Tables 2 and 5, we obtain 3σ upper limits of the fluxes to be 3.6×10^{-14} ergs cm $^{-2}$ s $^{-1}$ and 4.7×10^{-14} ergs cm $^{-2}$ s $^{-1}$ for N11 and N51D, respectively.

For N11, Maddox et al. (2009) claimed that the hard X-rays, detected at energies of up to ~ 7 keV, required a power-law component with a photon index of $\Gamma \sim 1.7$ and an observed flux of $\sim 3.0 \times 10^{-13}$ ergs cm $^{-2}$ s $^{-1}$ (in the 0.2–10 keV band)⁶. For N51D, the photon index and observed flux in the 0.3–3.0 keV band were reported to be $\Gamma \sim 1.3$ and $\sim 3.3 \times 10^{-13}$ ergs cm $^{-2}$ s $^{-1}$, respectively (Cooper et al. 2004). To directly compare these values with our results, these fluxes are modified to values in the 2–10 keV band, giving 2.3×10^{-13} ergs cm $^{-2}$ s $^{-1}$ for N11 and 7.1×10^{-13} ergs cm $^{-2}$ s $^{-1}$ for N51D. These values are about one order higher than the upper limits that we have obtained. The spectral models for the claimed hard X-ray emissions are shown in Figure 11 with black solid lines. Note that the point sources had been excluded from the EPIC spectrum of N51D (Cooper et al. 2004). Nevertheless, both models give fluxes clearly exceeding those given by the XIS spectrum in which the point-source fluxes are contained.

Given that the point-source flux in N11 is negligibly small (Fig. 11), the detection of hard X-rays claimed in the previous report was probably due to incorrect background subtraction. In fact, Maddox et al. (2009) commented that the subtraction of Ni lines originating from the NXB was unsuccessful. The NXB spectrum of the XIS consists of emission-line and continuum components, and their intensities are correlated with each other (Tawa et al. 2008). Therefore, this also caused the incomplete subtraction of the continuum component in the previous reports. In our analyses, on the other hand, the fluorescent NXB lines are accurately subtracted (see Section 3.3.1), and hence the background reduction is considered to be successful. The problem concerning N51D

⁶ The energy range from which the flux was derived is not given in Maddox et al. (2009). Therefore, we independently estimated it from reported values of the absorption column density, photon index, and the ratio of the observed to unabsorbed fluxes.

TABLE 7
COMPARISON OF NONTHERMAL LUMINOSITIES WITH OTHER SOURCES.

Object	L_X (ergs s $^{-1}$) ^a	Reference
N11	$< 1 \times 10^{34}$	This work.
N51D	$< 1 \times 10^{34}$	This work.
30 Dor C	2×10^{35}	Yamaguchi et al. (2009)
Arches	1×10^{34}	Tsujimoto et al. (2007)
NGC 6334	8×10^{32}	Ezoe et al. (2006)
RCW38	5×10^{32}	Wolk et al. (2002)
Westerlund 1	3×10^{34}	Muno et al. (2006)
Westerlund 2	2×10^{34}	Fujita et al. (2009)

NOTE. — ^aLuminosity in the 2–10 keV band.

is analogous to the case of N11, because the residual of the Al-K α line due to incomplete background subtraction has been reported (Cooper et al. 2004). We point out that the analysis of faint extended sources, such as SBs in the LMC, is very sensitive to the estimation of the NXB and the vignetting effect, and thus should be performed with great care.

Nonthermal X-ray emissions have so far been discovered from several Galactic star-forming regions, the Arches cluster (Tsujimoto et al. 2007), NGC 6334 (Ezoe et al. 2006), RCW 38 (Wolk et al. 2002), Westerlund 1 (Muno et al. 2006), and Westerlund 2 (Fujita et al. 2009). In these cases, however, the emissions are correlated with relatively compact (1–10-pc-scale) regions around an OB association or in a molecular cloud core. 30 Dor C is another example of a star-forming region that exhibits nonthermal (synchrotron) X-rays (Bamba et al. 2004). However, the X-ray shell can be interpreted as a single middle-aged SNR expanding rapidly inside the SB cavity (Yamaguchi et al. 2009). Therefore, at present, there is no evidence for large-scale (~ 100 pc) nonthermal emission distributed entirely in an SB. As given in Table 7, the luminosities of the nonthermal X-ray emissions in N11 and N51D are, if any, less than those of 30 Dor C and some of the other star-forming regions.

It is theoretically expected that efficient cosmic-ray acceleration can take place in SBs due to repeated SN shocks and/or magnetic turbulence (e.g., Bykov & Fleishman 1992; Parizot et al. 2004). Moreover, Butt & Bykov (2008) suggested that more than 10% of the

energy stored in an SB can be constantly transferred to accelerating cosmic-ray particles at the evolution stage of N11 and N51D (a few Myr). If this is the case, accelerated electrons would quickly lose their energies via radiation so that no nonthermal X-rays would be detected. It is still an open issue whether or not SBs can efficiently accelerate cosmic-rays, but this is beyond the scope of this paper. Future detailed observations and the development of theoretical models are required to solve this problem.

6. SUMMARY

We have analyzed the *Suzaku* XIS data of the extended X-ray emission from the SBs N11 and N51D. The analysis of the *XMM-Newton* EPIC data has also been performed to quantify the contribution from the point-like sources. In both SBs, the spectra of the diffuse components are well represented by thin thermal plasma at collisional ionization equilibrium. The electron temperatures derived for N11 and N51D are ~ 0.3 keV and ~ 0.2 keV, respectively. The elemental abundances are comparable with average LMC values, suggesting that the thermal emission mainly originates from the shock-heated ISM with only slight SN enrichment.

Neither N11 nor N51D show any evidence for hard X-ray emission, contrary to the previous claims

by Maddox et al. (2009) and Cooper et al. (2004). The 3σ upper limits of the 2–10 keV flux are 3.6×10^{-14} ergs cm $^{-2}$ s $^{-1}$ for N11 and 4.7×10^{-14} ergs cm $^{-2}$ s $^{-1}$ for N51D. The published claims of the detection of nonthermal X-rays are thought to be simply due to inadequate background subtraction. Careful analyses (i.e., NXB and point-source subtraction, vignetting correction, and so on) are required to obtain an accurate flux for faint extended sources, such as N11 and N51D. As the result of this work, no observational evidence for the nonthermal X-ray emission widely associated with SBs remains, with the exception of 30 Dor C (however, this is likely to be a single remnant of a recent SN explosion). It is still an open issue whether or not SBs can efficiently accelerate cosmic-rays. Observations of more SBs with longer exposures as well as the development of theoretical calculations are required.

We thank Yoshihiro Ueda for useful comments on the CXB. H.Y. is supported by the Special Postdoctoral Researchers Program in RIKEN, and the Grant-in-Aid for Young Scientists from the Ministry of Education, Culture, Sports, Science and Technology (MEXT) of Japan. M.S. is a Research Fellow of Japan Society for the Promotion of Science (JSPS).

REFERENCES

- Anders, E., & Grevesse, N. 1989, *Geochim. Cosmochim. Acta*, 53, 197
- Bamba, A., Ueno, M., Nakajima, H., & Koyama, K. 2004, *ApJ*, 602, 257
- Bomans, D. J., Rossa, J., Weis, K., & Dennerl, K. 2003, *A Massive Star Odyssey: From Main Sequence to Supernova*, 212, 637
- Butt, Y. M., & Bykov, A. M. 2008, *ApJ*, 677, L21
- Bykov, A. M., & Fleishman, G. D. 1992, *MNRAS*, 255, 269
- Chu, Y.-H., & Mac Low, M.-M. 1990, *ApJ*, 365, 510
- Cooper, R. L., Guerrero, M. A., Chu, Y.-H., Chen, C.-H. R., & Dunne, B. C. 2004, *ApJ*, 605, 751
- Dickey, J. M., & Lockman, F. J. 1990, *ARA&A*, 28, 215
- Dunne, B. C., Points, S. D., & Chu, Y.-H. 2001, *ApJS*, 136, 119
- Ezoe, Y., Kokubun, M., Makishima, K., Sekimoto, Y., & Matsuzaki, K. 2006, *ApJ*, 638, 860
- Fujita, Y., Hayashida, K., Takahashi, H., & Takahara, F. 2009, *PASJ*, 61, 1229
- Hatano, H., et al. 2006, *AJ*, 132, 2653
- Henize, K. G. 1956, *ApJS*, 2, 315
- Hughes, J. P., Hayashi, I., & Koyama, K. 1998, *ApJ*, 505, 732
- Koyama, K., et al. 2007, *PASJ*, 59, S23
- Lucke, P. B., & Hodge, P. W. 1970, *AJ*, 75, 171
- Mac Low, M.-M., Chang, T. H., Chu, Y.-H., Points, S. D., Smith, R. C., & Wakker, B. P. 1998, *ApJ*, 493, 260
- Mac Low, M.-M., & McCray, R. 1988, *ApJ*, 324, 776
- Maddox, L. A., Williams, R. M., Dunne, B. C., & Chu, Y.-H. 2009, *ApJ*, 699, 911
- McCray, R., & Snow, T. P., Jr. 1979, *ARA&A*, 17, 213
- Mitsuda, K., et al. 2007, *PASJ*, 59, S1
- Morrison, R., & McCammon, D. 1983, *ApJ*, 270, 119
- Muno, M. P., Law, C., Clark, J. S., Dougherty, S. M., de Grijs, R., Portegies Zwart, S., & Yusef-Zadeh, F. 2006, *ApJ*, 650, 203
- Nazé, Y., Antokhin, I. I., Rauw, G., Chu, Y.-H., Gosset, E., & Vreux, J.-M. 2004, *A&A*, 418, 841
- Oey, M. S., & Smedley, S. A. 1998, *AJ*, 116, 1263
- Parizot, E., Marcowith, A., van der Swaluw, E., Bykov, A. M., & Tatischeff, V. 2004, *A&A*, 424, 747
- Persson, S. E., Madore, B. F., Krzemiński, W., Freedman, W. L., Roth, M., & Murphy, D. C. 2004, *AJ*, 128, 2239
- Russell, S. C., & Dopita, M. A. 1992, *ApJ*, 384, 508
- Serlemitsos, P. J., et al. 2007, *PASJ*, 59, S9
- Smith, R. K., Brickhouse, N. S., Liedahl, D. A., & Raymond, J. C. 2001, *ApJ*, 556, L91
- Strüder, L. et al. 2001, *A&A*, 365, L18
- Tawa, N., et al. 2008, *PASJ*, 60, S11
- Tsujimoto, M., Hyodo, Y., & Koyama, K. 2007, *PASJ*, 59, 229
- Turner, M. J. L. et al. 2001, *A&A*, 365, L27
- Walborn, N. R., Drissen, L., Parker, J. W., Saha, A., MacKenty, J. W., & White, R. L. 1999, *AJ*, 118, 1684
- Walborn, N. R., & Parker, J. W. 1992, *ApJ*, 399, L87
- Weaver, R., McCray, R., Castor, J., Shapiro, P., & Moore, R. 1977, *ApJ*, 218, 377
- Wolk, S. J., Bourke, T. L., Smith, R. K., Spitzbart, B., & Alves, J. 2002, *ApJ*, 580, L1
- Yamaguchi, H., Bamba, A., & Koyama, K. 2009, *PASJ*, 61, 175